



## Label-free conduction velocity mapping and gap junction assessment of functional iPSC-Cardiomyocyte monolayers

Wenkun Dou<sup>a,1</sup>, Qili Zhao<sup>b,1</sup>, Manpreet Malhi<sup>c,d,1</sup>, Xingjian Liu<sup>a</sup>, Zhuoran Zhang<sup>a</sup>, Li Wang<sup>a</sup>, Stephane Masse<sup>g</sup>, Kumaraswamy Nanthakumar<sup>g</sup>, Robert Hamilton<sup>h</sup>, Jason T. Maynes<sup>c,d,i,\*</sup>, Yu Sun<sup>a,e,f,j,\*\*</sup>

<sup>a</sup> Department of Mechanical and Industrial Engineering, University of Toronto, Toronto, M5S 3G8, Canada

<sup>b</sup> Institute of Robotics and Automatic Information System and the Tianjin Key Laboratory of Intelligent Robotics, Nankai University, Tianjin, 300071, China

<sup>c</sup> Program in Molecular Medicine, Hospital for Sick Children, Toronto, M5G 1X8, Canada

<sup>d</sup> Department of Biochemistry, University of Toronto, Toronto, M5S 1A8, Canada

<sup>e</sup> Institute of Biomaterials and Biomedical Engineering, University of Toronto, Toronto, M5S 3G9, Canada

<sup>f</sup> Department of Electrical and Computer Engineering, University of Toronto, Toronto, M5S 3G4, Canada

<sup>g</sup> Toronto General Hospital, Toronto, M5G 2C4, Canada

<sup>h</sup> Program in Translational Medicine, Hospital for Sick Children, Toronto, M5G 1X8, Canada

<sup>i</sup> Department of Anesthesia and Pain Medicine, Hospital for Sick Children, Toronto, M5G 1X8, Canada

<sup>j</sup> Department of Computer Science, University of Toronto, Toronto, M5T 3A1, Canada

### ARTICLE INFO

#### Keywords:

Conduction velocity  
iPSC-cardiomyocyte  
Label-free mapping  
Beating trajectories  
Excitation-contraction coupling  
Arrhythmia

### ABSTRACT

Cardiac conduction is an important function of the heart. To date, accurate measurement of conduction velocity (CV) in vitro is hindered by the low spatial resolution and poor signal-to-noise ratio of microelectrode arrays (MEAs), or the cytotoxicity and end-point analysis of fluorescence optical imaging. Here, we have developed a new label-free method based on defocused brightfield imaging to quantify CV by analyzing centroid displacements and contraction trajectories of each cardiomyocyte in a monolayer of human stem cell-derived cardiomyocytes (iPSC-CMs). Our data revealed that the time delay between intracellular calcium release and the initiation of cell contraction is highly consistent across cardiomyocytes; however, the duration a cell takes to reach its maximum beating magnitude varies significantly, proving that the time delay in excitation-contraction coupling is largely constant in iPSC-CMs. Standard calcium imaging of the same iPSC-CM populations ( $\sim 10^6$  cells) was conducted for comparison with our label-free method. The results confirmed that our label-free method was capable of achieving highly accurate CV mapping ( $17.64 \pm 0.89$  cm/s vs.  $17.95 \pm 2.29$  cm/s,  $p$ -value  $> 0.1$ ). Additionally, our method effectively revealed various shapes in cell beating pattern. We also performed label-free CV mapping on disease-specific iPSC-CM monolayers with plakophilin-2 (PKP2) knockdown, which effectively quantified their low CV values and further validated the arrhythmogenic role of PKP2 mutation in arrhythmogenic right ventricular cardiomyopathy (ARVC) through the disruption of cardiac conduction. The label-free method offers a cytotoxic-free technique for long-term measurement of dynamic beating trajectories, beating propagation and conduction velocities of cardiomyocyte monolayers.

### 1. Introduction

Disorders that affect heart rhythm contribute significantly to the morbidity and mortality of heart disease (Benjamin et al., 2017). The underlying etiology and risk factors for the development of a cardiac

arrhythmia are multi-faceted, including hypertension, genetics, obesity and the presence of other existing cardiac diseases. Normal heart rhythm is established by pacemaker cells in the sinoatrial node, which spontaneously initiates the propagation of the cardiac action potential (AP) through the heart tissue, ensuring coordinated contraction and the

\* Corresponding author. Department of Anesthesia and Pain Medicine and Program in Molecular Medicine, Hospital for Sick Children, Toronto, M5G 1X8, Canada.

\*\* Corresponding author. Department of Mechanical and Industrial Engineering, University of Toronto, Toronto, M5S 3G8, Canada.

E-mail addresses: [jason.maynes@sickkids.ca](mailto:jason.maynes@sickkids.ca) (J.T. Maynes), [sun@mie.utoronto.ca](mailto:sun@mie.utoronto.ca) (Y. Sun).

<sup>1</sup> Authors contributed equally.

efficient expulsion of blood during the cardiac cycle. The speed and direction with which the AP wavefront progresses is referred to as the conduction velocity (CV) with deviations from the normal CV pattern associated with arrhythmia (i.e., cardiac fibrillation with a spiral-shaped CV pattern) (Haissaguerre et al., 2014; Nayak et al., 2017). A slowing of the CV can occur in the presence of cardiac fibrosis or with inherited arrhythmogenic diseases (Jamil-Copley et al., 2015), leading to an increased risk for aberrant wavefront generation and the establishment of a lethal cardiac arrhythmia (Chow et al., 2002; King et al., 2013). To delineate disease mechanisms and identify new potential therapeutic agents, pre-clinical methods that properly model and quantify the shape and speed of the CV are needed.

The generation of spontaneously beating cardiac monolayers from matured, induced pluripotent stem cell-derived cardiomyocytes (iPSC-CMs) facilitates the quantitative study of cell autonomous (i.e., ion channel) and cell non-autonomous (i.e., gap junction electrical signal propagation) contributions to cardiac electrophysiology, in cells containing a human proteome. Using these types of experimental systems, CV mapping was performed to model genetic and inherited aberrations to cardiac conduction, such as those seen in Arrhythmogenic Cardiomyopathy (ARVC), and for probing drug-induced electrical/rhythm alterations (either adverse changes or to identify potential therapeutics) (Asimaki et al., 2014; Campbell et al., 2012; Eloff et al., 2003). Since cardiac electrical signal propagation involves factors internal to the cardiomyocyte and contributors from neighboring cells, CV mapping informs on multiple components of cardiac tissue function, and can be performed on patient-specific (derived) cells.

The CV of cardiomyocyte monolayers is typically mapped using multielectrode arrays (MEAs). However, the spatial resolution of MEAs is limited by large interelectrode spacing ( $>100\ \mu\text{m}$ ) (Qian et al., 2017), restricting the application of traditional MEA devices in mapping the physiologically-relevant complex AP propagation patterns that can exist (Panfilov and Keener, 1995). Newer MEAs, based on complementary metal-oxide-semiconductor (CMOS) technology, with higher electrode density and lower pitch ( $<20\ \mu\text{m}$ ) (Ballini et al., 2014), suffer from high costs and poor signal-to-noise ratios (SNR), equally restricting their utility (Spira and Hai, 2013). Optical mapping using fluorescent dyes was also applied to CV measurements, often with single-pixel resolution, facilitating the description of more complex CV patterns, for instance, the first demonstration of spiral-shaped AP propagation (Gray et al., 1998) and quatrefoil reentry patterns (Lin et al., 1999). The most common dyes utilized for optical CV mapping are small molecules that quantify cellular voltage changes or calcium fluxes, but both sets of dyes have cytotoxicity and photobleaching issues (Larsen et al., 2012; Lin et al., 1999).

Here, we address the current technical limitations to the measurements of CV by developing a label-free technique using computer vision analysis. We illustrate that the simultaneous capture of multiple points of physical contraction within a monolayer construct of beating cardiomyocytes can be utilized to quantify CV, capitalizing on consistent cellular excitation-contraction coupling (correlation between electrical and physical cellular changes). We find that iPSC-CMs monolayers contract with four major trajectory shapes, and model the delayed CV seen in a form of Arrhythmogenic Cardiomyopathy (Gerull et al., 2004). Our newly described method facilitates label-free CV measurement that is not limited by spatial resolution or adverse perturbation to the tissue, allowing for disease modeling and the investigation of potential therapeutics.

## 2. Material and methods

### 2.1. Microscopy, imaging and stimulation instrumentation

The imaging system consists of a standard inverted microscope (Nikon TE2000-S, Nikon Microscopes); a camera (HiSpec 1, Fastec Imaging Corp) utilized to capture brightfield images under 4x (image size:

$896 \times 696$  pixels) at 1 kHz; and an electrode pair mounted on a micromanipulator (MX7600, Siskiyou Inc.).

Cardiomyocyte monolayers were electrically paced using a pair of silver rod electrodes with a diameter of  $100\ \mu\text{m}$  (Harvard Apparatus Canada). The pitch between the two electrodes was set to be  $100\ \mu\text{m}$ . The electrodes were moved by a micromanipulator into one well of the 96-well plate, adjusted to the same field of view with the monolayer of cells and then raised by  $10\ \mu\text{m}$  above the cell monolayer. The cardiomyocytes were paced by using rectangular monophasic pulses (2 ms pulse duration, 2 Hz, 10 V amplitude, Supplementary Fig. 4a). The generated electric field ( $3.45 \times 10^4\ \text{V/m}$ ) was sufficient for electrical pacing without evidence of cell damage (Hirt et al., 2014; Tandon et al., 2009). Finite element simulations were conducted in COMSOL Multiphysics (Comsol Inc., version 5.1) to estimate the generated electric field (Supplementary Fig. 4b).

### 2.2. Human iPSC-CM culturing

Monolayers of iPSC-CMs were cultured as per the previously described method (Wang et al., 2018). Briefly, iPSC-CMs (iCell2®, Cellular Dynamics International, Madison WI) were plated to 96-well plates coated with a matrix mixture consisting of fibronectin ( $10\ \mu\text{g/mL}$ ) (356,008, Corning), gelatin (0.1% w/v) (G1890, Sigma), and laminin ( $10\ \mu\text{g/mL}$ ) (CC095, Sigma) at a density of 40,000 cells per well. Following a seven-day culture period ( $37\ ^\circ\text{C}$ , 5%  $\text{CO}_2$ ), the cardiomyocytes formed a synchronously beating confluent monolayer.

### 2.3. PKP2 silencing

pGIPZ short hairpin RNA (shRNA) constructs targeting the plakophilin-2 (PKP2) gene were obtained from the GE Dharmacon library (GE Healthcare, United Kingdom) and packaged into lentivirus by SPARC BioCentre (The Hospital for Sick Children, Canada). Monolayers of iPSC-CMs were virally transduced, and transduction efficiency was monitored by GFP fluorescence. Knockdown at the protein level was confirmed two weeks post-transduction by Western blot using an anti-PKP2 mouse monoclonal antibody (ab151402) at 1:100 dilution.

### 2.4. Immunofluorescence staining

Cell locations and alignment of myofilaments were assessed by fluorescent microscopy. Following 7 days of culture on coated 96-well plates, the cells were fixed in 4% formaldehyde for 15 min, permeabilized with 0.1% Triton X-100 in TBS for 15 min, and blocked in fresh antibody diluent solution (5% goat serum in 0.01% Triton X-100) for 1 h at room temperature. The cells were then incubated with mouse-raised anti- $\alpha$ -actinin primary antibody (ab9465 Abcam, Canada) diluted at 1:500 in antibody diluent overnight at  $4\ ^\circ\text{C}$ , followed by Alexa Fluor 594 anti-mouse secondary antibody (4408 S, Cell Signaling Technology, Danvers, MA) at 1:1000 in antibody diluent with 1X Hoechst 33,342 (4082 S, Cell Signaling Technology, Danvers, MA) for 1 h at room temperature. Images were acquired on a Leica SP8 confocal microscope and analyzed in ImageJ (1.8, National Institutes of Health, USA).

### 2.5. Calcium imaging

iPSC-CMs were loaded with  $10\ \mu\text{M}$  fluo-4 acetoxymethyl ester (fluo-4 AM) in the presence of Pluronic F-127 (20% solution in DMSO, Invitrogen), and incubated in a humidified  $37\ ^\circ\text{C}$  incubator with 5%  $\text{CO}_2$  for 30 min. Subsequently, the cells were rewashed three times with dye-free medium. Fluorescence was excited at 488 nm and recorded at 520 nm. Fluorescence videos were captured on an Evolve TM 128 camera (Photometrics, USA).  $\text{Ca}^{2+}$  fluorescent images were analyzed in custom-developed Matlab (Mathworks, Natick, MA) software according to the reported method (Herron, 2016). In brief, calcium signals were temporally filtered with local regression using weighted linear least squares

and a first-order polynomial model. Images were spatially filtered using 2D median filtering. Transient fluctuation of cytosolic  $\text{Ca}^{2+}$  concentration was reported as  $\Delta F/F_0$ , where  $F_0$  was the baseline value with minimum fluorescent intensity and  $\Delta F$  was the intensity change for the selected region at each given time point. Time delays of  $\text{Ca}^{2+}$  wave propagation were fitted to a third-order polynomial surface. Calculation methods for the conduction velocity (speed and direction) at each cell location are detailed in the Supplementary Material.

## 2.6. Statistical analysis

Statistical analysis was performed using Origin 2018 software (Microcal, Northampton, MA, USA). Each set of data was from three to six experimental replicates and was presented as values of the mean and the standard error of the mean. For differential analysis, Student's t-test was used for two groups and ANOVA with a Tukey post hoc test was used for multiple comparisons.  $p$ -value < 0.05 or less was considered statistically significant.  $p$ -values were displayed graphically as follows: \*  $p$ -value < 0.05, \*\*  $p$ -value < 0.01, ns = not significant. All data sets passed Shapiro-Wilk normality tests and equal variance tests.

## 3. Results

### 3.1. Label-free cell identification and image segmentation of monolayer cardiomyocytes

For label-free CV analysis, the physical location of individual cardiomyocytes within a monolayer must be determined, a challenge given the flat, featureless, and continuous characteristics of the cells after they join to form functional tissue layers. Human iPSC-CMs were grown on a standard culture surface derivatized with a pre-determined mixture of extracellular matrix proteins (fibronectin 10  $\mu\text{g}/\text{mL}$ , laminin 10  $\mu\text{g}/\text{mL}$ , gelatin 0.1% w/v) in serum-depleted media. To facilitate directional CV measurement, silver pacing electrodes were used to stimulate the cell monolayer (Fig. 1a, Supplementary Fig. 4a). Action potential was initiated at the stimulating position (origin) and propagated throughout the cardiomyocyte monolayer using a square waveform (10 V, 2 Hz) (Ruan et al., 2016). Electrical stimulation was conducted for 1 min before cell imaging to synchronize and stabilize cell beating frequency to that of the simulation signals. To maintain a label-free system, cell beating behaviors were recorded by brightfield microscopy using a camera at 1 kHz (HiSpec 1, Fastec Imaging Corp). The position of the focusing plane (Fig. 1b) was set by determining the height at which a minimum value of the coefficient of variation of pixel intensity (Dehlinger et al., 2013) was obtained (the ratio of standard deviation to

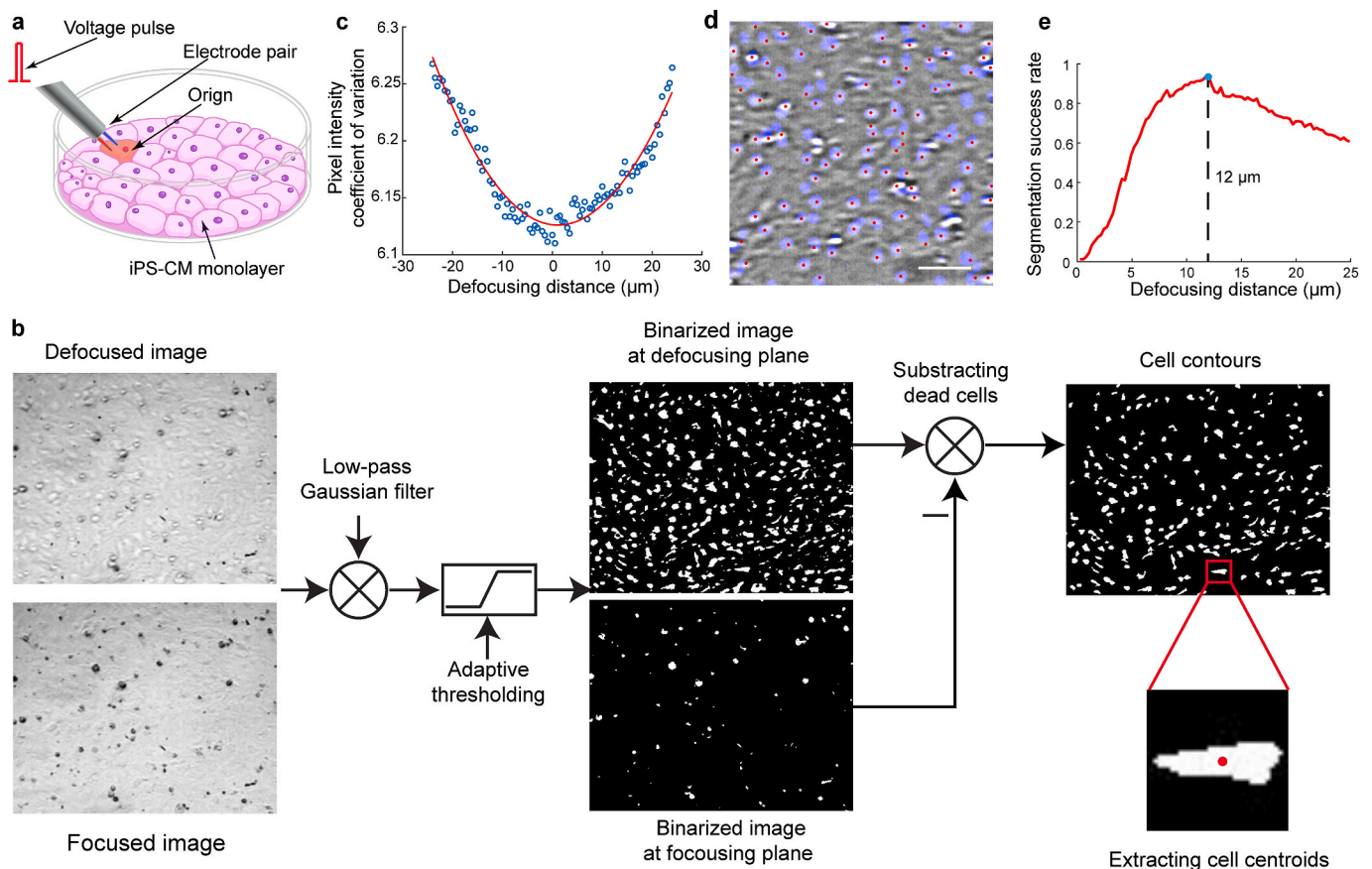


**Fig. 1.** System setup and image processing procedures for conduction velocity mapping. (a) Schematic of system setup. iPSC-CM monolayers were paced by a bipolar electrode with a frequency of 2 Hz and an amplitude of 10 V. Action potential was initiated at the origin and propagated throughout the monolayer. (b) The sequence of image processing for extracting cell centroids. Cardiomyocyte monolayers were imaged in both focusing and defocusing planes. The original images (only sub-region shown) were filtered and binarized to extract the contour and centroid of each cardiomyocyte. The focused image had low contrast, only detecting the low number of highly rounded cells that lost contractility and floated on the surface on cell monolayer. Those cells were subtracted from the binarized defocused image to reduce mapping error. (c) Coefficient of pixel intensity with respect to the defocusing distance. The focus plane was determined with the minimum value of the coefficient of variation of pixel intensity. (d) Cell locations in the same region of cardiomyocyte monolayer that were detected by fluorescent DAPI staining (blue) and label-free method (cell centroid, red). (e) Segmentation success rates under different defocused distances. The highest success rate (91%) was obtained at the defocusing distance of 12  $\mu\text{m}$ . (For interpretation of the references to colour in this figure legend, the reader is referred to the Web version of this article.)

mean, Fig. 1c). Due to their thin, flattened geometry and high degree of confluency, cardiomyocytes in a cell monolayer showed minimal or no individual features in the focusing plane, with only non-adhered cells singularly identifiable (highly rounded shape above the beating plane, Fig. 1b and Supplementary Fig. 1a). Some non-adhered cells are expected when a high plating density is used to ensure tissue confluency. We capitalized on the presence and lack of spontaneous beating (as individual cells) of these non-adhered entities, detecting them in the focused image by Hough-transform-based circle detection (Cheng et al., 2009) for subtraction from the subsequent cell segmentation process to improve CV mapping accuracy.

To improve image contrast for cell segmentation, we employed defocusing microscopy (see Supplementary information for imaging mechanism). In the defocused state, cells bend light by refraction, creating a sufficient brightness difference between the cell center and boundary areas for cell separation (Fig. 1a). In the defocusing plane, the center area of each cardiomyocyte was more easily segmented with standard image processing techniques, including steps of image enhancement, binarization, contour detection, and subtraction of the non-adhered cardiomyocytes that were previously detected in the focusing plane (source code available for downloading at <https://github.com/WenkunDou/Label-Free-Conduction-Velocity-Mapping>).

Because image quality is highly sensitive to the focal height, the optimal defocusing plane for cell segmentation was determined by imaging cardiomyocyte monolayers at multiple focal heights. The number of nuclei quantified by fluorescent staining (DAPI) in the same imaging area was set as a benchmark, and the success rate for cell segmentation was calculated by normalizing the number of the segmented cells in the defocused image to the benchmark value at each defocusing distance (Fig. 1d and e and Supplementary Fig. 1). The highest segmentation success rate with a defocusing distance of 12  $\mu\text{m}$  (Fig. 1e) was used in subsequent experiments to detect cell contours, track beating trajectories and calculate the corresponding CV of iPSC-CM monolayers.

The segmentation efficiency of the defocused brightfield imaging method was compared with phase contrast microscopy (Mann et al., 2005) and differential interference contrast microscopy (DIC) (Arnison et al., 2004) (Supplementary Fig. 3). Phase contrast and DIC imaging are commonly used to enhance the contrast between transparent cells and background by converting the invisible phase shifts in light when passing through a transparent specimen into brightness changes through interference (Thorn, 2016). Phase shift in light is produced by the thickness and refractive index differences between single cells/cell clusters and their surrounding background. However, since cardiomyocytes in a monolayer are tightly attached to each other, little background or cell boundaries are exposed, leading to the low contrast of cardiomyocytes in monolayers. In addition, the inherent side illumination effect of DIC caused heterogeneity in image intensity (Supplementary Fig. 3b). The segmentation success rates of phase contrast and DIC were 17.53% and 24.86%, respectively vs. the success rate of 91.65% using defocusing microscopy (Supplementary Fig. 3c). For the small fraction of cells that were not successfully segmented by the defocused imaging method, confounding factors were binucleation of cardiomyocytes (Bergmann et al., 2009; Korbassi et al., 2020) and cardiomyocytes occluded by dead cells that floated on the cell monolayer. Nevertheless, our label-free method was capable of successfully distinguishing more than 90% of the cell population and sufficed [the continuity of beating propagation and CV mapping on cardiomyocyte monolayers.

### 3.2. Determining cardiomyocyte beating trajectories and centroid displacements

Silver pacing electrodes were utilized to initiate synchronous beating at a defined position on the iPSC-CM monolayer for CV mapping (interelectrode distance: 100  $\mu\text{m}$ ; frequency: 2 Hz; amplitude: 10 V). Finite element simulation was conducted to determine the electric field

between the two electrodes (Supplementary Fig. 4b). The maximal magnitude of the electric field ( $3.45 \times 10^4$  V/m, sufficient for electrical pacing (Hirt et al., 2014)) was located at the midpoint of the two electrode tips and regarded as the origin of action potential propagation. Positions of cell centroids were calculated from the segmented cell contours (Supplementary information for detection of cell centroid). In the beating cardiomyocyte monolayer, we observed that contraction leads to the movement of a cell centroid away from its start-beating position, with reliable return during relaxation. To analyze the beating behavior of individual cardiomyocytes in a monolayer, both the trajectories of cardiomyocyte centroids and the centroid displacements in the XY-plane were captured using a 4X objective (0.13 NA, Nikon) and measured with a subpixel resolution of 0.14  $\mu\text{m}$  (see Supplementary Information for details). The timepoint at which cells reached their maximum centroid displacement was used to isolate the contraction and relaxation period during each beating cycle.

Measured maximum centroid displacements (i.e. beating magnitudes) ranged from 0 to 2.4  $\mu\text{m}$ , with an average value of  $0.93 \pm 0.53$   $\mu\text{m}$  ( $n = 288$  cells) (Fig. 2g). Interestingly, diverse cardiomyocyte trajectories were observed (Fig. 2a–f; Supplementary Videos 1–5), with approximately 9% of cells having no apparent beating cycles (Fig. 2a). Since these cells exhibited minute random trajectories near their static position with a displacement amplitude smaller than 0.2  $\mu\text{m}$ , they were excluded from CV mapping. Other cardiomyocytes were classified into two groups according to the number of peaks on their centroid displacement curves during one beating period. About 80% of the cardiomyocytes had a single displacement peak, with subdivision into line (35%, Fig. 2b, Video 1), oval (24%, Fig. 2c, Video 2), triangular (11%, Fig. 2d, Video 3), and figure-8 (10%, Fig. 2e, Video 4) shaped displacements. Approximately 11% of the cardiomyocytes had more than one displacement peak (Fig. 2f, Video 5). Cells with multiple peaks had the same beating frequency as the pacing signal (2 Hz), indicating that they were paced successfully and should be included in CV mapping. Fig. 2h shows that the different beating trajectories were randomly distributed in the monolayer, suggesting that the trajectory findings were generalizable and not limited to microenvironments or induced by experimental artifact. The relative scarcity and random placement of statically beating cells, which were excluded from subsequent CV analysis, did not influence the continuity of surface fitting for CV mapping.

Supplementary video related to this article can be found at <https://doi.org/10.1016/j.bios.2020.112468>.

### 3.3. Mapping tissue monolayer conduction velocity

Under the defined electrical pacing protocol, beating initiated at the origin location and propagated to other cardiomyocytes throughout the monolayer. Considering the 0.14  $\mu\text{m}$  resolution in cell centroid displacement measurement, we defined the timepoint when a cell centroid moved greater than 0.2  $\mu\text{m}$  from its start-beating position as the start time for cell contraction. For cells with a single displacement peak, the peak time was defined as the timepoint when the cell reached its maximum centroid displacement (Fig. 3a). For cells with multiple displacement peaks, parabolic curve fitting was performed to locate the equivalent peak time (Fig. 3b). The start time and peak time were measured for each cell and compared to the corresponding start/peak time obtained at the origin during the same beating cycle to determine the time delay ( $\Delta t$ ) of cell beating. The time delay values were then fit into a third-order polynomial surface ( $R^2 > 0.97$  for all monolayers) (Fig. 3c). At each cell location, the CV value was calculated based on  $\Delta t$  and the distance from the origin (see Supplementary Information for calculation).

Typical CV mapping results comparing start-times and peak-times are shown in Fig. 3d and e. To correlate internal changes in ion fluxes to the observed cellular physical contraction (excitation-contraction coupling), the CV and  $\Delta t$  values at the same cell locations were also

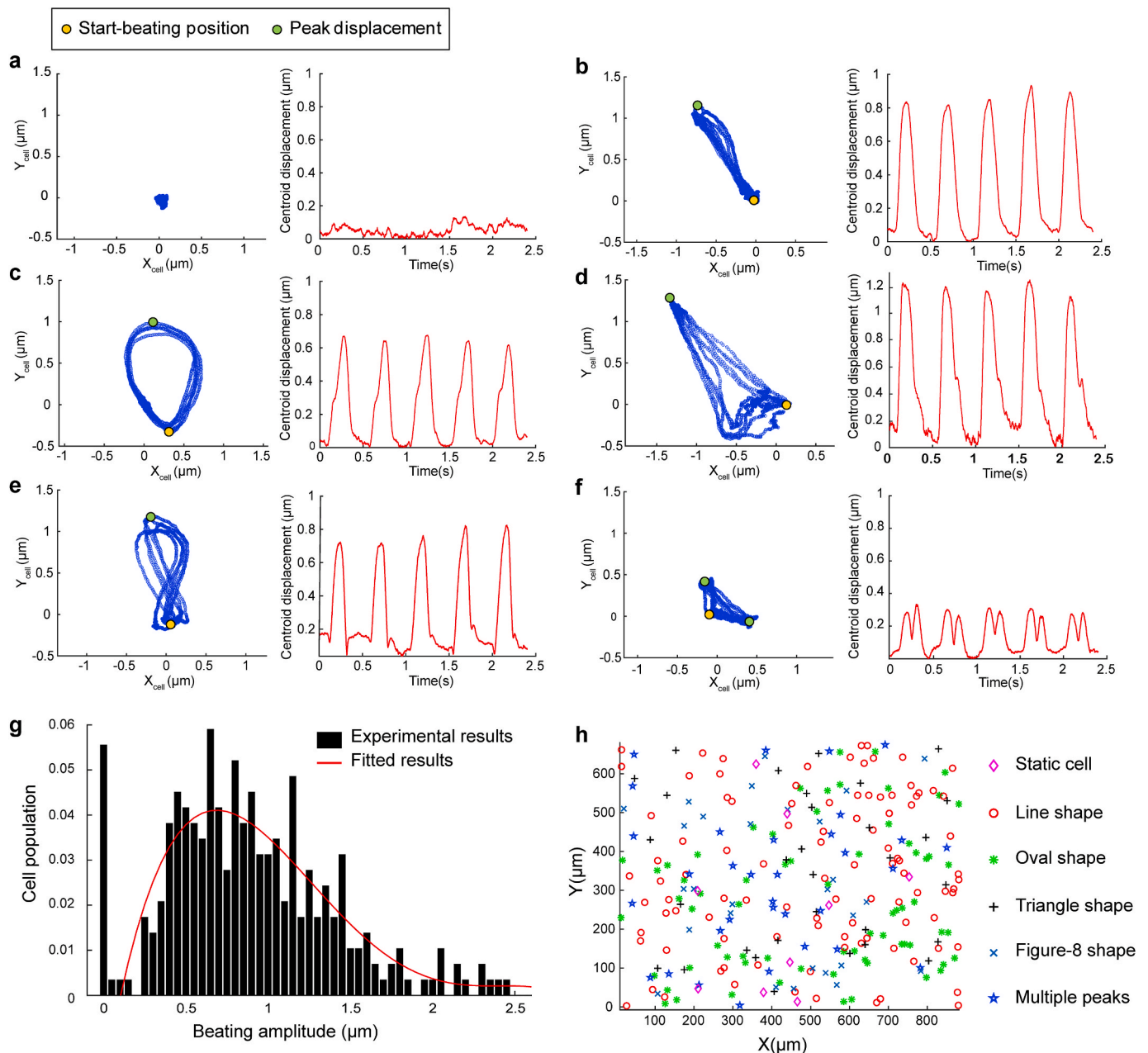


**Fig. 2.** Trajectories and displacements of cell centroids. (a) The trajectory and centroid displacement curve of cardiomyocytes whose centroids stayed at the static position with no apparent beating cycle and centroid displacement. (b–e) Trajectories and centroid displacements of cardiomyocytes with a single displacement peak during each beating cycle. Yellow dot represents the static position and green dot represents cell centroid positions with maximum displacement. (f) The trajectory and centroid displacement of cells with multiple peaks during each beating cycle. (g) Statistical distribution of maximum centroid displacements of cells. (h) Spatial distribution of cardiomyocytes with different trajectory shapes. (For interpretation of the references to colour in this figure legend, the reader is referred to the Web version of this article.)

measured by calcium imaging (Lee et al., 2012) (Fig. 3f). We found that the CV obtained utilizing contraction start-time comparisons was consistent with the results obtained from calcium imaging ( $17.64 \pm 0.89$  cm/s vs.  $17.95 \pm 2.29$  cm/s,  $p$ -value > 0.1,  $n = 941$ ). However, the CV calculated by comparing contraction peak-times significantly deviated from these groups ( $22.75 \pm 8.21$  cm/s,  $n = 941$ ). The relative error was defined as the relative difference of CV values between the start/peak-time methods and the corresponding calcium mapping results at each cell position. Error maps (Supplementary Fig. 5) show that the relative errors of all cell locations measured by the start-time method ( $5.63\% \pm 0.70\%$ ) were much lower than those measured by the peak-time method ( $29.19\% \pm 3.57\%$ ).

Typically, maximum cytosolic  $\text{Ca}^{2+}$  concentration is observed 4 ms after the beginning of  $\text{Ca}^{2+}$  release from SR (Bers, 2002), ensuring the temporal coupling of the calcium peak and the initiation of cell contraction. We analyzed the calcium-contraction coupling by recording the brightfield cell contraction and the fluorescent  $\text{Ca}^{2+}$  change consecutively, coinciding the calcium peak time and the start-beating time of the cell at origin, and calculating the difference between the time of calcium peak and the start-beating time at multiple tissue locations. We found that this time interval was consistently  $0.003 \pm 0.02$  ms throughout the monolayer, confirming a largely constant time interval between the calcium peak time and the start time of cell contraction (Fig. 3i). Thus, compared with CV results from the standard

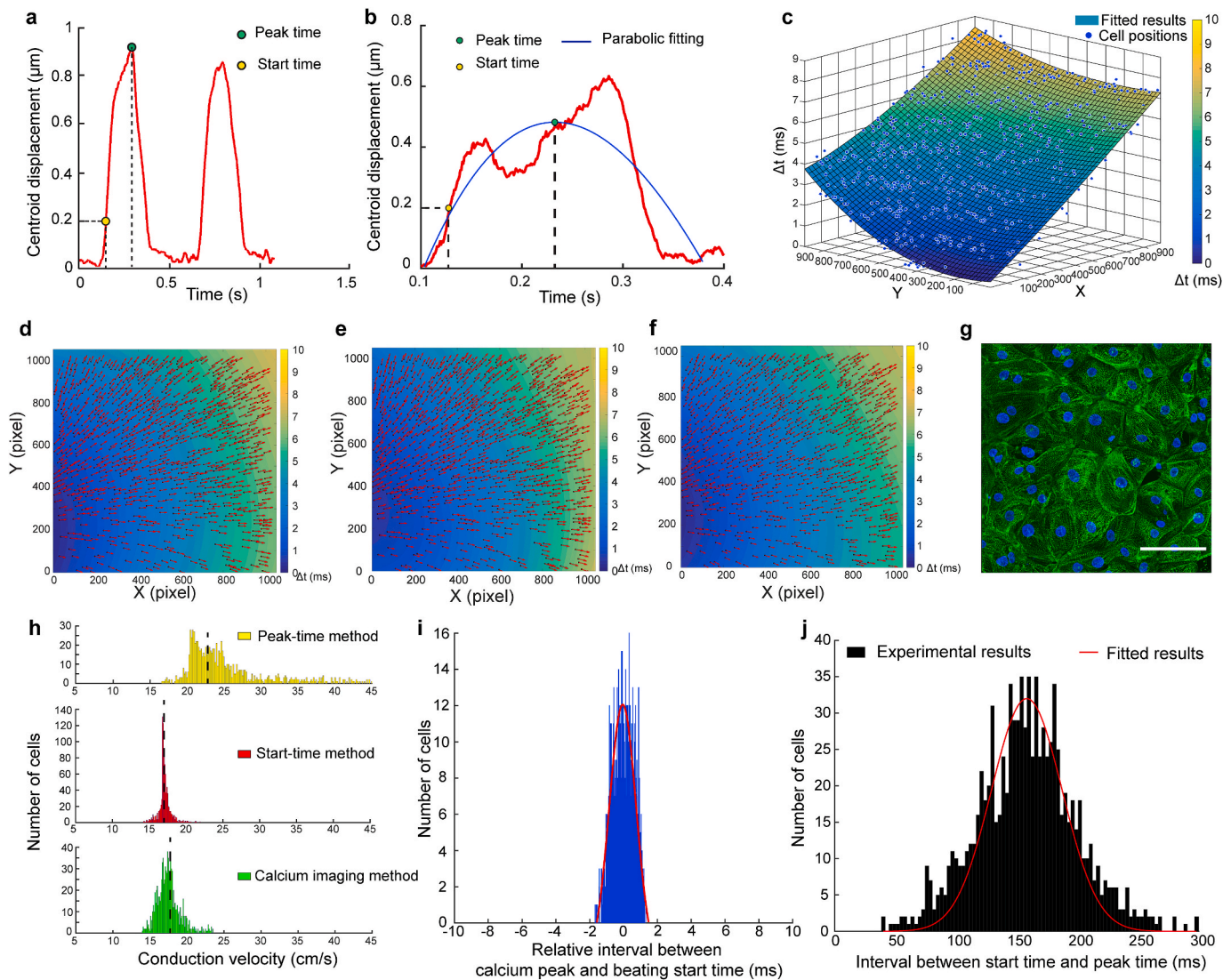


**Fig. 3.** Comparison of CV mapping results by label-free and standard calcium imaging methods. (a,b) Defining the *start time* and the *peak time* on centroid displacement curves with single or multiple displacement peaks. Start time is defined as the timepoint when cell centroid moves  $0.2 \mu\text{m}$  from the start-beating position. Peak time is defined as the timepoint when cell reaches the maximum centroid displacement. (b) Parabolic fitting was conducted to locate the peak time for cells with multiple displacement peaks. (c) Time delay of beating propagation fitted to a third-order polynomial surface for CV calculation. (d,e,f) Conduction velocity map of the same iPSC-CM monolayer measured by the *start-time* method, the *peak-time* method, and the standard calcium imaging method. Color represents the time delay of cell beatings at different cell locations during a single beating cycle. The length and direction of each red arrow represent the magnitude and direction of the CV value at each cell position. The calcium imaging map was used as benchmark. (g) Immunostaining of  $\alpha$ -actinin (green) revealed the diversity of cell shapes and myofibril alignments among the iPSC-CMs. (h) Distributions of CV values measured on the same iPSC-CM monolayer by the *start-time* method, the *peak-time* method, and calcium imaging. Dash lines represent the mean CV value. (i) Distribution of relative time intervals between the calcium peak time and the start time of cell contraction of the measured iPSC-CMs. (j) Distribution of time intervals between the start and peak time of the measured iPSC-CMs. (For interpretation of the references to colour in this figure legend, the reader is referred to the Web version of this article.)

calcium mapping method, the relative errors caused by following contraction start-times were insignificant. The conduction velocity magnitudes of cardiomyocytes with different trajectory shapes show no statistical significance (Supplementary Fig. 6). Likely due to the non-perfect alignment of myofilaments between cells and slightly variant cell shapes (Fig. 3g), we found variations in the time interval between the start and peak times of cell contraction across the monolayer (Fig. 3j), resulting in a large variance in CV mapping when comparing peak contraction times. These results prove that the time delay between intracellular calcium release and the initiation of cell contraction (i.e., *excitation-contraction* coupling) is highly consistent across cardiomyocytes; however, the duration a cell takes to reach its maximum beating magnitude varies.

### 3.4. Extended term label-free CV measurement

For disease modeling and potential therapeutic screening, an extended duration of testing provides essential information about temporal variations in the CV and the spontaneous generation of irregular beating patterns. Extended testing is particularly challenging when dye- or label-based methods are utilized with changes to cell physiology/health induced by the label, coupled with signal degradation over time. We compared our label-free method of CV mapping to dye-based calcium imaging for measurement consistency over time. We observed that CV values remained constant over 120 min of continuous measurement using our label-free method (Fig. 4a). Although the CV values were statistically the same at the beginning of the experiment, when comparing label-free and calcium flux measurements, the average CV

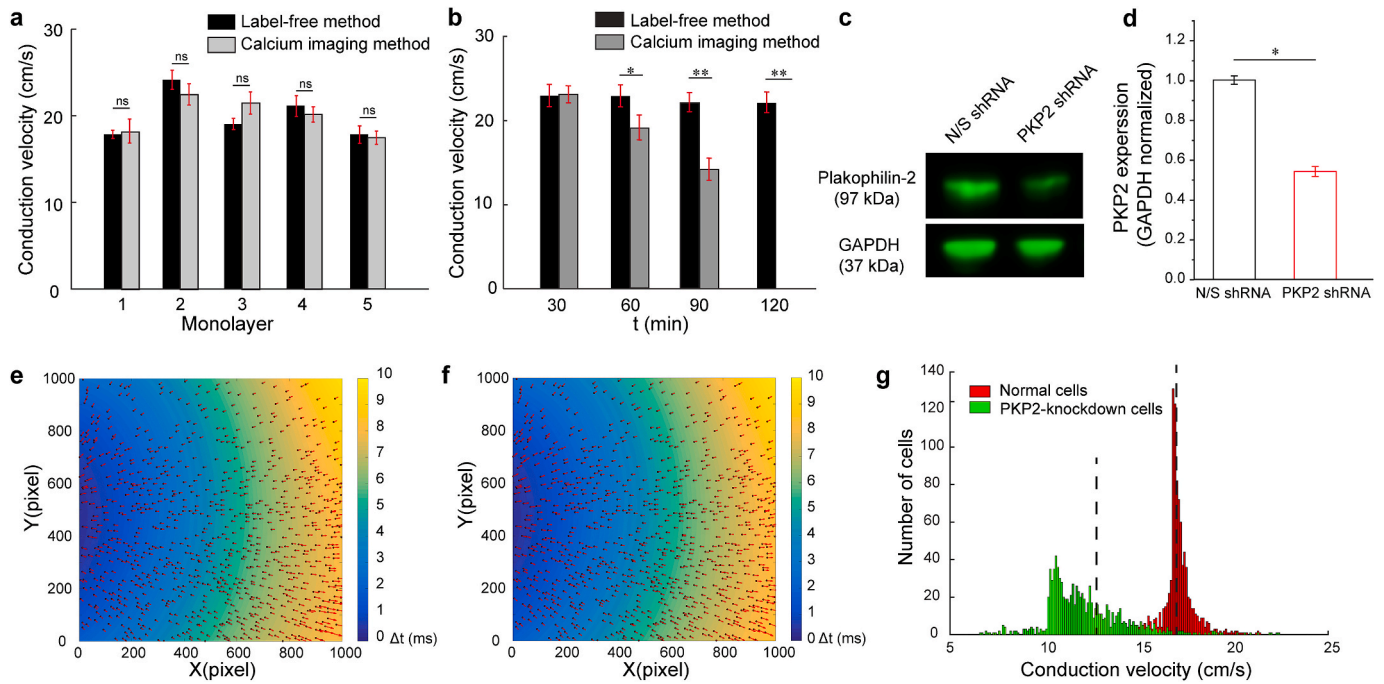


**Fig. 4.** Testing the label-free CV measurement in a disease model. (a) Conduction velocities of iPSC-CM monolayers measured by the label-free method and the calcium imaging method. Results showed no significant difference between the methods ( $p$ -value  $> 0.1$ ). (b) CV values measured overtime illustrating degradation of the calcium measurement. The CV results as measured by the label-free method showed stability over the same duration. (c,d) Representative Western blot bands and quantification of PKP2 expression levels in PKP2 knock-down iPSC-CM monolayers. (e,f) CV map of electrically paced PKP2-knockdown cardiomyocytes measured by (e) the label free method and (f) the calcium imaging method. (g) CV distributions of PKP2-knockdown and normal iPSC-CMs. Dash lines represented the mean CV value.  $n = 3$  monolayers for (a,b,d). Error bars represent standard error of mean; \*,  $p$ -value  $< 0.05$ ; \*\*,  $p$ -value  $< 0.01$ .

values measured by calcium imaging decreased by 38.05% at 90 min and dropped to 0 at 120 min (Fig. 4b). At 120 min, iPSC-CM monolayers showed a flat calcium fluorescent intensity without dynamic change, indicating the disruption of intracellular calcium dynamics and cytotoxicity caused by the fluorescent dye. These results confirmed that the label-free method, which avoids the need for cytotoxic dyes or probes, is suitable for long-term CV measurement or monitoring.

### 3.5. CV mapping in a disease model of Arrhythmogenic Cardiomyopathy

Plakophilin-2 (PKP2) provides a key protein component of gap junctions, which are critical for forming the electrical connections between cardiomyocytes. Mutations in PKP2 that decrease protein function or level are common in ARVC, inducing adverse changes to gap junction function and electrical signal propagation (Oxford et al., 2007). Monolayers of iPSC-CMs were transduced with a lentivirus containing a PKP2-silencing sequence (shRNA-PKP2), resulting in a  $45 \pm 2\%$  reduction in PKP2 expression measured 12 days after viral transduction (Fig. 4c and d).

The CV of PKP2 knockdown iPSC-CM monolayers was measured by our label-free method and compared to calcium imaging (Fig. 4e and f). We found, as expected, that reduction of cellular PKP2 levels reduced the CV of the monolayers, consistent with the known pathology of ARVC (non-silencing control CV  $17.09 \pm 0.92$  cm/s vs.  $12.96 \pm 4.53$  cm/s,  $n = 905$ ). CV values from our label-free method were not statistically different from the values determined by calcium imaging ( $12.96 \pm 4.53$  cm/s vs.  $12.75 \pm 3.94$  cm/s,  $p$ -value  $> 0.1$ ,  $n = 864$  cells) with a relative mapping error of  $3.88 \pm 1.71\%$  (Supplementary Fig. 7a). Approximately 80% cardiomyocytes of PKP2-knockdown hiPSC-CMs had a single displacement peak, similar to the non-silencing hiPSC-CMs (Supplementary Fig. 7b). However, PKP2-knockdown hiPSC-CMs revealed differences in the shape of trajectories (Supplementary Fig. 7c). Additionally, PKP2 knockdown increased the spatial variance of the CV values, indicating different conduction properties across cell layer

(Fig. 4g). This finding is particularly interesting given the unpredictable and stochastic induction of lethal arrhythmias that occurs in ARVC.

## 4. Discussions

For proper function, the heart requires the consistency of two electrical systems: the membrane depolarization and internal flow of ions that induces cell-based contraction, and the traveling, coordinated electrical signal that ensures the proper propagation and timing of cardiac (organ) contraction. While the former can be studied at the cell level, making analysis and therapeutic discovery somewhat less challenging (i.e., high-throughput patch clamping), the latter requires the quantification of signal propagation (the CV) from cell-to-cell in a physiologically-relevant way. Although many cardiac diseases result from derangements in the conduction of electrical signals, necessitating therapeutic discovery, most current methods for measuring the CV utilize dyes or probes, and often disturb the conduction itself or are cytotoxic.

Calcium imaging is commonly used for measuring calcium dynamics and the CV of cardiac tissue (Li et al., 2007). Our results highlight the detrimental effect of long-term calcium imaging by quantitatively showing disruption of calcium dynamics and CV over time (Fig. 4b). Cells imaged at 60 or 90 min following dye loading showed decreases in CV by 16.47% and 38.05%, respectively. Furthermore, both dynamic changes in fluorescence intensity and cell beating ceased 120 min after dye loading, demonstrating the severe influence of calcium dyes on cardiac electrophysiology and contractility, likely through reactive oxygen species (ROS) generation and the chelation of available calcium ions (Herron et al., 2012). By comparison, our label-free method obtained consistent CV values during 120 min of mapping and did not affect cell beating behaviors. Our method circumvents the disadvantages of cytotoxicity and end-point analysis associated with calcium imaging, confirming its suitability for long-term and repetitive CV measurement of iPSC-CM monolayers. This capability is important for investigating

the development of conduction properties in cardiomyocytes during the maturation process of iPSC-CMs, and for therapeutic discovery, given the inherently stochastic processes involved in arrhythmogenesis.

Our technique also identified and classified different types of beating trajectories of the cardiomyocyte monolayers, relevant to the generation of arrhythmic beats in the heart. We observed that approximately 80% of the cardiomyocytes had a single displacement peak with four types of beating trajectories, namely, line- (Fig. 2b, Video 1), oval- (Fig. 2c, Video 2), triangular- (Fig. 2d, Video 3) and figure-of-eight-shaped (Fig. 2e, Video 4). Meanwhile, a small number of cardiomyocytes showed double displacement peaks (11%, Fig. 2f, Video 5) or no obvious centroid displacement (9%, Fig. 2a). We also found that beating amplitudes ranged from 0 to 2.4  $\mu\text{m}$  (Fig. 2g), and that the time intervals between the start and peak time of centroid displacement distributed between 43 ms and 300 ms (Fig. 3j). We speculate that the diversity of centroid trajectories, beating amplitudes and time intervals were influenced by cell shape and myofilament alignment. In human heart tissues, adult cardiomyocytes have an anisotropic rod-like shape with an aspect ratio of 7:1 to 9.5:1 (Feric and Radisic, 2016). However, as shown in Fig. 3g, iPSC-CMs were distributed throughout the field of view with different cell shapes and sometimes regionally random myofilament directions (despite an established maturation protocol that includes electrical stimulation (Tandon et al., 2009)). Myofilament directions inside the cardiomyocytes have been reported to be determined by the cell shape and the cell aspect ratio in vitro (Bray et al., 2008). In general, iPSC-CMs in a monolayer are expected to exhibit more uniform centroid trajectories, beating amplitudes and beating time intervals by improving myofilament alignment. Our results reveal that the time interval between intracellular calcium release and the initiation of cell contraction is highly consistent across cardiomyocytes, indicating that the time delay in excitation-contraction coupling is largely constant in iPSC-CM monolayers. Our label-free method aims at the conduction velocity (CV) measurement of 2D cardiomyocyte monolayers through detecting the beating trajectories and centroid displacements of individual cells. In terms of 3D cardiac tissues, their complex three dimensional cell-cell connections, low transparency and large-scale motion pose difficulties to cell detection, cell segmentation and the tracking of cell beating trajectories, making our method unsuitable for CV mapping of 3D cardiac tissues.

Human iPSC-derived cardiomyocytes are a powerful tool for modeling patient-specific diseases in vitro, investigating disease mechanisms, screening new drugs and developing regenerative therapies (Meer et al., 2016). Genetically modified or patient-derived iPSC-CMs have been shown to recapitulate the electrophysiological phenotype of specific diseases, such as long QT syndrome (Lahti et al., 2012), LEOPARD syndrome (Carvajal-Vergara et al., 2010) and diabetic cardiomyopathy (Drawnel et al., 2014). Mutations of PKP2 was found in patients with arrhythmogenic right ventricular cardiomyopathy (APVC), an inherited disease that presents with sudden and unexpected sustained ventricular arrhythmia and possibly death (Van Tintelen et al., 2006). Pathological mutation of PKP2 (either functionally lost or lower/nil protein expression) leads to a structural disruption of gap junction plaques, resulting in the loss of gap junction-mediated electrical communication between cells (Oxford et al., 2007). shRNA knockdown of PKP2 in neonatal rat ventricular myocytes was previously found to disrupt electrical coupling and reduce the speed of AP propagation, consistent with the human disease phenotype (Oxford et al., 2007; Sato et al., 2009). Our label-free CV mapping supports the disruptive effects of PKP2 mutation on cardiac conduction (PKP2-knockdown decreased CV by 24.2% relative to cells treated with a non-silencing control). By comparing the CV values at each cell location, we showed that PKP2-deficient cell populations exhibited an inconsistency in cardiac conduction, revealed by larger standard deviations (4.53 cm/s vs. 0.92 cm/s) and scattered CV distributions (Fig. 4g). These unique intracellular communication phenotypes provide a basis for therapeutic evaluation using our label-free CV mapping method.

## 5. Conclusion

We report a label-free method for the extended measurement of cardiac conduction velocity by mapping the beating propagation of cardiomyocytes in functionally beating monolayers. For the first time, we were able to show unique types of beating trajectories of cell centroids. CV values measured by our technique ( $17.95 \pm 2.29$  cm/s) were not statistically different from CV measured by the more traditional approach of calcium imaging ( $17.64 \pm 0.89$  cm/s) but were consistent over time without an effect on the cell itself. Our results revealed a constant time interval between the peak intracellular calcium concentration and the initiation of cell contraction. We were able to demonstrate a clinically-relevant arrhythmogenic phenotype and reduced CV in cells with knockdown of PKP2, a key protein often mutated in arrhythmogenic cardiomyopathies. Our method offers a unique tool to provide information about cardiomyocyte beating behaviors (amplitude, centroid trajectories), beating propagation and CV. The label-free characteristic of our technique avoids the perturbation and cytotoxicity induced by fluorescent dyes, while the capability for extended-term measurement enables future translational applications, such as monitoring CV changes induced by disease-relevant genetic mutations or for therapeutic evaluation.

## CRedit authorship contribution statement

**Wenkun Dou:** Conceptualization, Investigation, Methodology, Data curation, Writing - original draft. **Qili Zhao:** Conceptualization, Methodology, Data curation, Software, Writing - original draft. **Manpreet Malhi:** Methodology, Investigation, Data curation, Writing - original draft. **Xingjian Liu:** Data curation, Software. **Zhuoran Zhang:** Methodology, Validation. **Li Wang:** Investigation, Visualization. **Stephane Masse:** Methodology, Visualization. **Kumaraswamy Nanthakumar:** Methodology, Visualization. **Robert Hamilton:** Methodology, Validation. **Jason T. Maynes:** Resources, Validation, Supervision, Writing - review & editing. **Yu Sun:** Conceptualization, Resources, Validation, Supervision, Writing - review & editing, Project administration.

## Declaration of competing interest

The authors declare that they have no known competing financial interests or personal relationships that could have appeared to influence the work reported in this paper.

## Acknowledgments

The authors acknowledge the financial support from the Canadian Institutes of Health Research (CIHR) and the Natural Sciences and Engineering Research Council of Canada (NSERC) through a Collaborative Health Research Projects (CHRP) grant. Y.S. also acknowledges the financial support from the Canada Research Chairs Program and the Ontario Research Fund – Research Excellence Program. W.K.D. acknowledges a fellowship from the Ted Rogers Center for Heart Research Education Fund. J.T.M. would like to thank his clinical colleagues for protected time, and the Wasser Family and the SickKidsFoundation for Chair funds.

## Appendix A. Supplementary data

Supplementary data to this article can be found online at <https://doi.org/10.1016/j.bios.2020.112468>.

## References

- Arnison, M.R., Larkin, K.G., Sheppard, C.J.R., Smith, N.I., Cogswell, C.J., 2004. *J. Microsc.* 214, 7–12.

- Asimaki, A., Kapoor, S., Plovie, E., Arndt, A.K., Adams, E., Liu, Z.Z., James, C.A., Judge, D.P., Calkins, H., Churko, J., Wu, J.C., MacRae, C.A., Kléber, A.G., Saffitz, J. E., 2014. *Sci. Transl. Med.* 6 (240), 240ra74-240ra74.
- Ballini, M., Muller, J., Livi, P., Chen, Y., Frey, U., Stettler, A., Shadmani, A., Viswam, V., Jones, I.L., Jackel, D., Radivojevic, M., Lewandowska, M.K., Gong, W., Fiscella, M., Bakkum, D.J., Heer, F., Hierlemann, A., 2014. *IEEE J. Solid State Circ.* 49, 2705–2719.
- Benjamin, E.J., Blaha, M.J., Chiuve, S.E., Cushman, M., Das, S.R., Deo, R., De Ferranti, S. D., Floyd, J., Fornage, M., Gillespie, C., Isasi, C.R., 2017. *Circulation* 135 (10), e146–e603.
- Bergmann, O., Bhardwaj, R.D., Bernard, S., Zdunek, S., Barnabé-Heider, F., Walsh, S., Zupicich, J., Alkass, K., Buchholz, B.A., Druid, H., Jovinge, S., 2009. *Science* 324 (5923), 98–102.
- Bers, D.M., 2002. *Nature* 415, 198–205.
- Bray, M.A., Sheehy, S.P., Parker, K.K., 2008. *Cell Motil Cytoskeleton* 65, 641–651.
- Campbell, K., Calvo, C.J., Mironov, S., Herron, T., Berenfeld, O., Jalife, J., 2012. *J. Physiol.* 590, 6363–6379.
- Carvajal-Vergara, X., Sevilla, A., Dsouza, S.L., Ang, Y.S., Schaniel, C., Lee, D.F., Yang, L., Kaplan, A.D., Adler, E.D., Rozov, R., Ge, Y., Cohen, N., Edelmann, L.J., Chang, B., Waghay, A., Su, J., Pardo, S., Lichtenbelt, K.D., Tartaglia, M., Gelb, B.D., Lemischka, I.R., 2010. *Nature* 465, 808–812.
- Cheng, H.D., Guo, Y., Zhang, Y., 2009. *Pattern Recogn.* 42, 1959–1969.
- Chow, A.W.C., Schilling, R.J., Davies, D.W., Peters, N.S., 2002. *Circulation* 105, 2172–2178.
- Dehlinger, D., Suer, L., Elsheikh, M., Peña, J., Naraghi-Arani, P., 2013. *Biotechnol. Bioeng.* 110, 838–847.
- Drawnel, F.M., Boccardo, S., Prummer, M., Delobel, F., Graff, A., Weber, M., Gérard, R., Badi, L., Kam-Thong, T., Bu, L., Jiang, X., Hoflack, J.C., Kiiäläinen, A., Jeworutzki, E., Aoyama, N., Carlson, C., Burcin, M., Gromo, G., Boehringer, M., Stahlberg, H., Hall, B.J., Magnone, M.C., Kolaja, K., Chien, K.R., Bailly, J., Iacone, R., 2014. *Cell Rep.* 9, 810–820.
- Eloff, B.C., Gilat, E., Wan, X., Rosenbaum, D.S., 2003. *Circulation* 108, 3157–3163.
- Feric, N.T., Radisic, M., 2016. *Adv. Drug Deliv. Rev.* 96, 110–134.
- Gerull, B., Heuser, A., Wichter, T., Paul, M., Basson, C.T., McDermott, D.A., Lerman, B.B., Markowitz, S.M., Ellinor, P.T., MacRae, C.A., Peters, S., 2004. *Nat. Genet.* 36 (11), 1162–1164.
- Gray, R.A., Pertsov, M., A, Jalife, J., 1998. *Nature* 392 (6671), 75–78.
- Haissaguerre, M., Hocini, M., Denis, A., Shah, A.J., Komatsu, Y., Yamashita, S., Daly, M., Amraoui, S., Zellerhoff, S., Picat, M.Q., Quotb, A., Jesel, L., Lim, H., Ploux, S., Bordachar, P., Attuel, G., Meillet, V., Ritter, P., Derval, N., Sacher, F., Bernus, O., Cochet, H., Jais, P., Dubois, R., 2014. *Circulation* 130, 530–538.
- Herron, T.J., 2016. *Cell Calcium* 59, 84–90.
- Herron, T.J., Lee, P., Jalife, J., 2012. *Circ. Res.* 110, 609–623.
- Hirt, M.N., Boeddinghaus, J., Mitchell, A., Schaaf, S., Börnchen, C., Müller, C., Schulz, H., Hubner, N., Stenzig, J., Stoehr, A., Neuber, C., Eder, A., Luther, P.K., Hansen, A., Eschenhagen, T., 2014. *J. Mol. Cell. Cardiol.* 74, 151–161.
- Jamil-Copley, S., Vergara, P., Carbuicchio, C., Linton, N., Koa-Wing, M., Luther, V., Francis, D.P., Peters, N.S., Davies, D.W., Tondo, C., Bella, P. Della, Kanagaratnam, P., 2015. *Circ. Arrhythmia Electrophysiol* 8, 76–86.
- Karbassi, E., Fenix, A., Marchiano, S., Muraoka, N., Nakamura, K., Yang, X., Murry, C.E., 2020. *Nat. Rev. Cardiol.* 1–19.
- King, J.H., Huang, C.L., Fraser, J.A., 2013. *Front. Physiol.* 4, 154.
- Lahti, A.L., Kujala, V.J., Chapman, H., Koivisto, A.-P., Pekkanen-Mattila, M., Kerkela, E., Hyttinen, J., Kontula, K., Swan, H., Conklin, B.R., Yamanaka, S., Silvennoinen, O., Aalto-Setälä, K., 2012. *Dis. Model. Mech.* 5, 220–230.
- Larsen, A.P., Sciuto, K.J., Moreno, A.P., Poelzing, S., 2012. *Heart Rhythm* 9, 1493–1500.
- Lee, P., Klos, M., Bollensdorff, C., Hou, L., Ewart, P., Kamp, T.J., Zhang, J., Bizy, A., Guerrero-Serna, G., Kohl, P., Jalife, J., Herron, T.J., 2012. *Circ. Res.* 110, 1556–1563.
- Li, X., Huang, J., Tibbits, G.F., Li, P.C.H., 2007. *Electrophoresis* 28, 4723–4733.
- Lin, S.F., Roth, B.J., Wikswo, J.P., 1999. *J. Cardiovasc. Electrophysiol.* 10, 574–586.
- Mann, C.J., Yu, L., Lo, C.-M., Kim, M.K., 2005. *Optic Express* 13, 8693.
- Meer, B.J., Tertoolen, L.G.J., Mummery, C.L., 2016. *Stem Cell.* 34, 2008–2015.
- Nayak, A.R., Panfilov, A.V., Pandit, R., 2017. *Phys. Rev. E* 95 (2), 022405.
- Oxford, E.M., Musa, H., Maass, K., Coombs, W., Taffet, S.M., Delmar, M., 2007. 703–711.
- Panfilov, A., Keener, J.P., 1995. *Chaos, Solit. Fractals* 5, 681–689.
- Qian, F., Huang, C., Lin, Y.D., Ivanovskaya, A.N., O'Hara, T.J., Booth, R.H., Creek, C.J., Enright, H.A., Soscia, D.A., Belle, A.M., Liao, R., Lightstone, F.C., Kulp, K.S., Wheeler, E.K., 2017. *Lab Chip* 17, 1732–1739.
- Ruan, J.L., Tulloch, N.L., Razumova, M.V., Saiget, M., Muskheili, V., Pabon, L., Reinecke, H., Regnier, M., Murry, C.E., 2016. *Circulation* 134, 1557–1567.
- Sato, P.Y., Musa, H., Coombs, W., Guerrero-Serna, G., Patino, G.A., Taffet, S.M., Isom, L. L., Delmar, M., 2009. *Circ. Res.* 105 (6), 523–526.
- Spira, M.E., Hai, A., 2013. *Nat. Nanotechnol.* 8, 83–94.
- Tandon, N., Cannizzaro, C., Chao, P.-H.G., Maidhof, R., Marsano, A., Au, H.T.H., Radisic, M., Vunjak-Novakovic, G., 2009. *Nat. Protoc.* 4, 155–173.
- Thorn, K., 2016. *Mol. Biol. Cell* 27, 219–222.
- Van Tintelen, J.P., Entius, M.M., Bhuiyan, Z.A., Jongbloed, R., Wiesfeld, A.C.P., Wilde, A. A.M., Van Der Smagt, J., Boven, L.G., Mannens, M.M.A.M., Van Langen, I.M., Hofstra, R.M.W., Otterspoor, L.C., Doevendans, P.A.F.M., Rodriguez, L.M., Van Gelder, I.C., Hauer, R.N.W., 2006. *Circulation* 113, 1650–1658.
- Wang, L., Dou, W., Malhi, M., Zhu, M., Liu, H., Plakhotnik, J., Xu, Z., Zhao, Q., Chen, J., Chen, S., Hamilton, R., Simmons, C.A., Maynes, J.T., Sun, Y., 2018. *ACS Appl. Mater. Interfaces* 10, 21173–21183.